Research Article

Power loss transition of stable ZnO varistor ceramics: Role of oxygen adsorption on the stability of interface states at the grain boundary

Zhuolin Cheng[a], Rou Li[a], Yiwei Long[b], Jianying Li[a],
Shengtao Li[a], Kangning Wu[a,*]

[a]*State Key Laboratory of Electrical Insulation and Power Equipment, Xi'an Jiaotong University, Xi'an 710049, China*
[b]*Department of Thermal and Fluid Engineering, University of Twente, Enschede 7500AE, the Netherlands*

Abstract: Highly stable ZnO varistor ceramics with steadily decreasing power loss have been put into applications in electrical and electronic systems for overvoltage protections, even with the absence of general understandings on their aging behaviors. In this paper, we investigated their aging nature via conducting comparative direct current (DC) aging experiments both in air and in nitrogen, during which variations of electrical properties and interface properties were measured and analyzed. Notably, continuously increasing power loss with severe electrical degradation was observed for the sample aged in nitrogen. The power loss transition was discovered to be closely related to the consumption of oxygen adsorption at the grain boundary (GB), which could, however, remain constant for the sample aged in air. The interface density of states (DOS) N_i, which is crucial for pinning the potential barrier, was proved to decrease in nitrogen, but keep stable in air. Therefore, it is concluded that the oxygen adsorption at the GB is significant for the stability of interface states, which further correlates to the long-term stability of modern stable ZnO varistor ceramics.

Keywords: ZnO varistor ceramics; aging; power loss; oxygen adsorption; interface states

1 Introduction

ZnO varistor ceramics are fundamental materials for metal-oxide arresters (MOAs), which are widely used for overvoltage protections in electrical systems and surge protections in the electronic industry because of their excellent nonlinear current density–electrical field (*J–E*) characteristics [1–3]. Since they are connected in parallel to electrical and electronic devices, aging of ZnO varistor ceramics is unavoidable during the long-term operation, resulting in the increase in power loss and deterioration in electrical properties [4,5]. The increasing power loss of ZnO varistor ceramics, as a threat to the electrical and electronic system, has been thoroughly investigated, which could be well explained by the classic ion migration model [6]. Unfortunately, the aging of recently developed stable ZnO varistor ceramics follows a completely different aging pattern. They show a decreasing power loss with aging time *t*, implying a lower risk of thermal runaway and an

* Corresponding author.
E-mail: wukning@xjtu.edu.cn

enhancement in the long-term stability [7,8]. It puzzles the industry and academic communities greatly since aging generally leads to the degradation of most dielectrics [2,9]. Moreover, the absence of their aging insights directly leads to troubles in condition assessments [10], especially when they are extensively put into industrial applications. Therefore, as acknowledged by the International Council on Large Electric systems (CIGRE) both in 2013 and 2017 [7,8], there is a critical need to understand what provides modern stable ZnO varistor ceramics with a decreasing power loss trend.

Interface properties are the key to determining the electrical properties of dielectrics [11–14]. The double Schottky barriers (DSBs) at grain boundaries (GBs) consisting of depletion layers and interface states are the foundation of nonlinear characteristics of ZnO varistor ceramics [15–22]. The depletion layers are composed of positive donor ions, such as singly-charged zinc interstitial $Zn_i^{\cdot}$, doubly-charged zinc interstitial $Zn_i^{\cdot\cdot}$, and oxygen vacancy $V_O^{\cdot}$ [6]. The negative interface states are possibly related to the sub-nanometer-thick oxygen enrichments at GB interfaces [2,11]. The electrical degradation of ZnO varistor ceramics essentially comes from the deformation of the DSB [23,24]. The classic ion migration model describes the process of positive migration ions neutralizing negative interface states under the electric field [6]. The model could well apply to traditional instable samples because of its predictions of the reduction in barrier height (ϕ_b) and the increase in power loss during aging. However, the aging of stable ZnO varistor ceramics cannot be explained by this classic model. Facing this challenge, we recently proposed a donor ion redistribution (DIR) model and simulated the carrier transport in a DSB by including the effect of donor redistribution with stable interface states at GBs [25,26]. The decreasing power loss and evolution of *J–E* characteristics of stable samples were theoretically reproduced during aging. However, more experimental evidence and discussions are critically needed to validate the stability of interface states and their related chemical origins.

Oxygen has been reported to play an important role at the GB interface of polycrystalline ceramics by creating a negative interface at GBs [2,11]. Peng *et al.* [27] ascribed the enhancement in electrical properties of ZnO-based varistors to the increase in oxygen adsorption at GBs. Bueno *et al.* [28] reported that the nonlinear coefficients of SnO$_2$-based varistors were reduced during thermal treatment in nitrogen. Moreover, the degradation could almost be restored by thermal treatment in an oxygen-rich atmosphere. Stucki and Greuter [29] found that the electrical properties of instable ZnO varistor ceramics degraded with the consumption of excess oxygen at GBs under heavy electrical stress, during which reductions in potential barriers and interface density of states (DOS) N_i were also reported. Overall, these models confirm the significant effect of GB oxygen on the stability of ZnO varistor ceramics. However, they are proposed on the basis of the experimental results of traditional instable samples. They cannot be directly used to explain the decreasing power loss of stable samples. Since atmospheres could influence the GB oxygen, conducting atmospheric direct current (DC) aging is thereby rewarding for understanding the aging stability of stable samples.

In this study, the stable sample with the decreasing power loss would exhibit instable aging behaviors with continuously increasing power loss and severe electrical degradation during aging in nitrogen. The transition caused by the nitrogen-rich atmosphere is found to be correlated with the consumption of oxygen adsorption at GBs, which then leads to the decrease in density of lower-lying interface states and the deformation of the DSB. The findings of this paper could help build in-depth understandings on the aging of stable ZnO varistor ceramics, and improve their long-term stability in the future.

2　Experimental

Commercial stable ZnO varistor ceramics (Xi'an Shendian Electric Co., Ltd., China) produced in the same batch were employed for atmospheric aging experiments in air and nitrogen. They were produced by sintering pure ZnO powders with metal-oxide dopants like Bi$_2$O$_3$, Co$_2$O$_3$, Sb$_2$O$_3$, and MnO$_2$. The samples were 38.0 mm in diameter and 12.5 mm in height *h*. The relatively harsh DC aging was carried out in an oven (DZ-1BCIV, Taisite, China) with controlled atmosphere a controlled atmosphere oven at 120 ℃ under 0.8 times of the breakdown voltage U_{1mA} (the voltage at 1 mA/cm^2). After aging, the DC voltage was

removed immediately, and the samples were recovered in air at the aging temperature. By using the atmospheric aging system (Fig. 1), the power loss and nonlinear *J*–*E* characteristics were measured *in situ* during aging. The DC aging part includes a DC voltage source (HB-Z502-50AC, HBGY, China) and a digital multimeter (8145C, VICTOR, China). The *J*–*E* characteristic measurement part consists of a DC voltage supply (TD2200, Teslaman, China) and a digital multimeter (DMM 7510, Keithley, USA). The atmosphere was controlled by continuous air or nitrogen flow, which was provided by a gas supply system (GSL-2Z, HF-Kejing, China) at a flow rate of 220 mL/min.

The amount of GB oxygen before aging and after recovery was obtained by using the X-ray photoelectron spectrometer (ESCALAB Xi+, Thermo Fisher Scientific, USA). The GB fractures were available by breaking these samples with ultrahigh instantaneous mechanical stress. The elemental analysis was performed on those fractures by the energy dispersive spectrometer (GeminiSEM 500, ZEISS, Germany) for verifying the accessibility of the GB surface. The depth profiles of the fracture surfaces were obtained during the X-ray photoelectron spectroscopy (XPS) test by mild sputtering with 500 eV Ar ions on the fracture surface. Moreover, the discrepancies of interface states between the unaged and recovered samples were investigated by a *J*–*E* deconvolution method combined with the capacitance–voltage technique by an impedance analyzer (Concept 43, Novocontrol, Germany). For the capacitance–voltage characteristic measurement, the DC voltages ranging from 100 to 1600 V were subsequently applied on the samples at 25 ℃. The GB capacitance was measured from 1 to 10^4 Hz under a small alternative current (AC) signal of 3 Vrms.
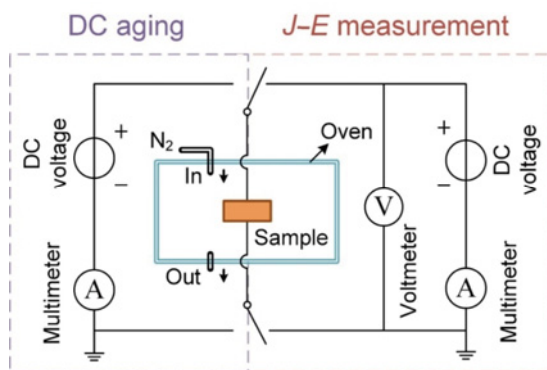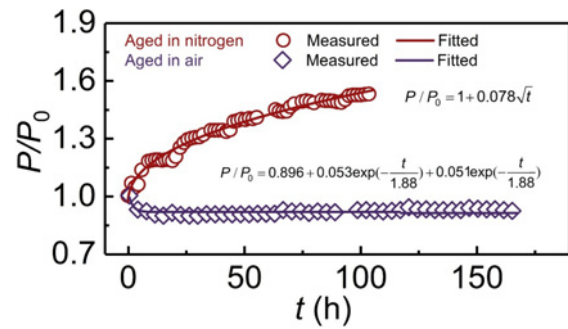

Fig. 1   Schematic diagram of DC aging system.

Fig. 2   Dependence of normalized power loss on *t* of ZnO varistor ceramics aged in air and aged in nitrogen. Note: *P* and P_0 are the measured power loss during the aging process and the power loss at *t* = 0 h, respectively.

3   Results and discussion

3.1   Transition of power loss

The dependence of normalized power losses on *t* for samples aged in air and in nitrogen is shown in Fig. 2. Notably, these two identical samples present completely different aging power loss trends due to the change in the atmosphere. On the one hand, the sample aged in air shows a decreasing power loss, which could be approximately fitted by a double exponential function of *t*. On the other hand, the sample aged in nitrogen exhibits a continuously increasing power loss, which has a linear relationship with the square of the aging time $t^{1/2}$. The fitting equations for their power losses are demonstrated in Fig. 2. For the sample aged in nitrogen, the increase in power loss follows the aging pattern of instable ZnO varistor ceramics, which show a reduction in ϕ_b, according to the thermionic emission theory [25,30].

$$J = A^* T^2 \mathrm{e}^{-\frac{q\phi_b + \xi_b}{kT}} \left(1 - \mathrm{e}^{-\frac{qU}{kT}} \right) \qquad (1)$$

where A^* (= 30 A/(cm^2·K^2)) is the effective Richard constant, *q* is the elementary charge, ξ_b (= 0.067 eV) is the bulk Fermi level relative to the conduction band, *k* is the Boltzmann constant, *T* is the absolute temperature, and *U* is the applied voltage. According to the DIR model [25,26], the power loss trend is the result of competition between DIR and the consumption of the interface states. The power loss transition in nitrogen originates from the dominance of interface states consumption, which leads to the deformation of the DSB. Reasonably, other factors like elevated aging

temperatures might also lead to a similar transition.

The evolution of *J*–*E* curves (Figs. 3(a) and 3(c)) also shows obvious differences due to the atmospheric effect. For the sample aged in air, small distortions are observed in both forward and reverse directions, showing a good long-term stability. Here, forward is the same direction as the applied DC voltage, and vice versa. However, severer degradation is observed in the sample aged in nitrogen, even though the *t* is only 106 h. Both their forward and reverse *J*–*E* curves move to the high-current region with the increase of *t*. Greater deformation of *J*–*E* curves in the reverse direction is found since the reverse-direction side sustains almost all the aging voltage.

Furthermore, variations in electrical parameters of samples aged in air and in nitrogen are calculated to demonstrate the changes caused by the power loss transition, as shown in Figs. 3(b) and 3(d), respectively. Electrical properties, including α (= $1/\log(U_{1mA}/U_{0.1mA})$, where $U_{0.1mA}$ is the voltage at 1 mA/cm^2), E_b (= U_{1mA}/h), and J_L (the current density under $0.75U_{1mA}$), are derived from the nonlinear *J*–*E* characteristics [31–33]. As for the sample aged in air, small changes in E_b, α, and J_L are observed in the reverse direction. However, the sample aged in nitrogen exhibits significant electrical degradation, particularly in the first 50 h. In the reverse direction, α drops sharply from 23.0 to 6.7, and J_L increases from 22.5 to 118.5 mA/cm^2. The transition of aging behaviors for the stable sample aged in nitrogen could be supported by the classic ion migration model, suggesting the destruction of their long-term stability caused by the oxygen-deficient atmosphere.

To further unveil the effects of atmospheric aging, DC voltages were removed for subsequent recovery experiments at the same temperature. The recovering behaviors of the two aging cases are depicted in Fig. 4. Complete recovery of stable samples aged in air is found in Fig. 4(a). After 509 h of recovery, the *J*–*E* characteristics in both forward and reverse directions almost overlap with their unaged *J*–*E* characteristics. The total recovery could also be proven by their recovered electrical parameters (Fig. 4(b)), where the gray dashed lines imply their initial unaged values. Electrical parameters of α, E_b, and J_L show rapid recovery in the first 2 h, and subsequently approach their unaged values at 509 h. The recovery thereby indicates the existence of stable interface states in stable ZnO varistor ceramics. The minor variations in *J*–*E* curves and electrical parameters result from the donor redistribution effect in depletion layers [25,26].
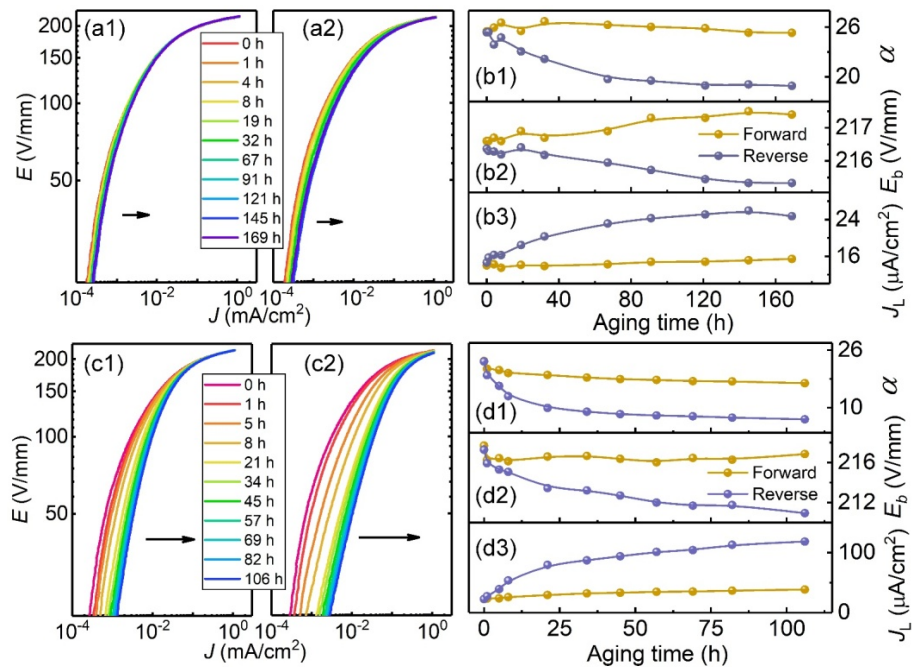
Fig. 3 Nonlinear *J*–*E* characteristics in (a1) forward and (a2) reverse directions and (b1–b3) variations in electrical parameters during being aged in air. Nonlinear *J*–*E* characteristics in (c1) forward and (c2) reverse directions and (d1–d3) variations in electrical parameters during being aged in nitrogen. Note: α, E_b, and J_L are the nonlinear coefficient, breakdown electric field strength, and leakage current density, respectively.
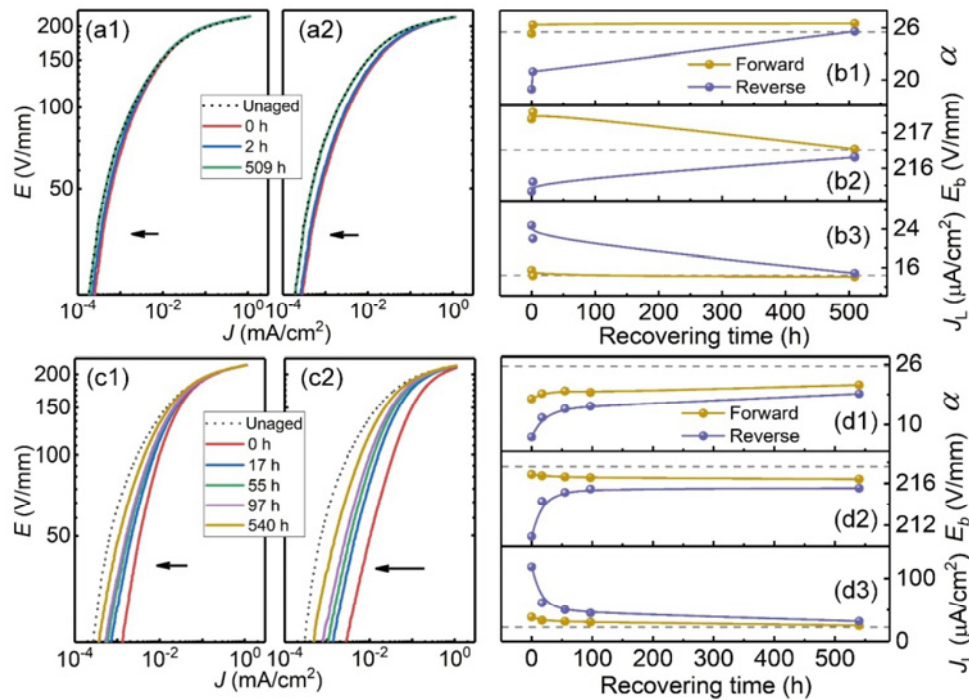
Fig. 4   Recovery of nonlinear *J–E* characteristics in (a1) forward and (a2) reverse directions and (b1–b3) electrical parameters after aged in air. Recovery of nonlinear *J–E* characteristics in (c1) forward and (c2) reverse directions and (d1–d3) electrical parameters after aged in nitrogen.

On the contrary, irreversibility in aging for the sample aged in nitrogen is found by its nonlinear *J–E* characteristics and electrical properties, as shown in Fig. 4(c). The *J–E* curves could recover to nearly symmetry in the forward and reverse directions. However, they are far from their unaged shapes, even after recovering for 540 h. In addition, the recovering trends of their electrical parameters (Fig. 4(d)) depart from their unaged values, which are represented by the gray dashed lines. The irreversible aging could be explained by the ion migration model, which states that positive mobile ions move towards GBs, and neutralize with the negative interface states. The destructed interface states thereby result in irreversible electrical properties. However, the chemical origin, which results in the destruction of interface states and the observed power loss transition, needs further discussions.

### 3. 2   Oxygen adsorption at GBs

In order to further understand the effect of nitrogen on the stability of stable ZnO varistor ceramics, the amount of GB oxygen, which is closely related to the electrical performance of ZnO varistor ceramics, was characterized through conducting the XPS etching experiments [11,29]. Since etching is a destructive

experiment, only unaged and recovered samples were investigated. The prepared fractures were firstly employed for the energy dispersive spectroscopy (EDS) measurements to ensure that GB surfaces were available. Figure 5(a) shows the elemental distributions of the selected area in the SEM image. The weight percentages of these elements are given as Zn (51.25 wt%), O (6.60 wt%), Bi (19.52 wt%), Co (12.59 wt%), and Sb (5.15 wt%). Significantly, Bi takes a large weight percentage despite small weight percentages in the grain [34]. Moreover, the availability of GB surfaces is also supported by the depth profile of fracture surfaces, as displayed in Fig. 5(b). The normalized Zn 2p continuously increases with the etching time, while the GB element Bi decreases due to etching from GBs to grains. It should be noted that the percentages of Zn 2p, O 1s, and Bi 4f keep almost unchanged from 150 to 300 s due to etching into the grains.

The depth profiles of O 1s spectra were investigated in detail. Firstly, the depth profiles of O 1s spectra from an unaged stable sample are plotted in Fig. 6(a), where two peaks at around 530 and 539 eV can be seen. The peak at 539 eV is related to the Sb $3d_{3/2}$ signal due to the addition of Sb_2O_3. The peak at 530 eV is mainly composited of O 1s signals, i.e., O 1s(I) and O 1s(II).
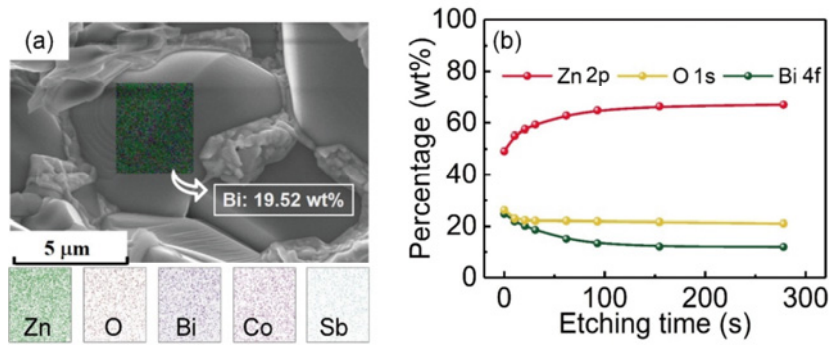
Fig. 5　(a) EDS analysis of GB fractures. (b) Dependence of normalized weight percentages of Zn 2p, O 1s, and Bi 4f on the etching time.
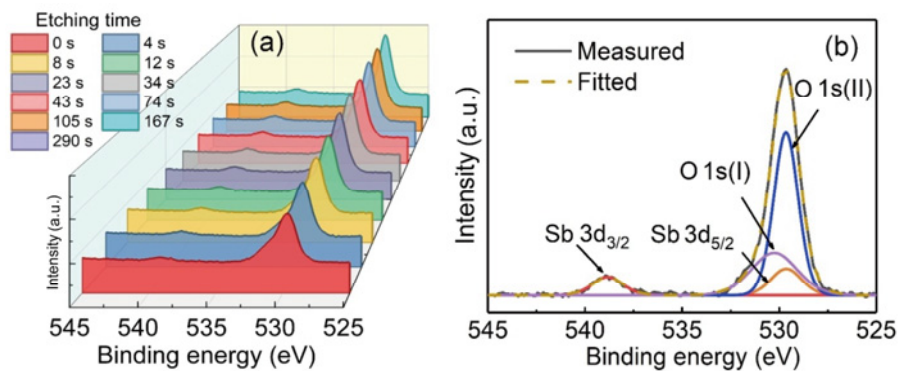

Fig. 6　(a) Depth profiles of O 1s XPS spectra and (b) experimental and decomposed peaks of O 1s and Sb 3d spectra for unaged stable ZnO varistor ceramics.

However, it also includes a small Sb 3d$_{5/2}$ signal due to the spin–orbit coupling effect. The two Sb signals should be excluded before analyzing the O 1s signals. Specifically, the area ratio of Sb 3d$_{5/2}$ and Sb 3d$_{3/2}$ is fixed to 3/2 with their doublet splitting energy of about 9 eV [35,36]. After excluding Sb signals, the remaining O 1s(I) and O 1s(II) signals are fitted by Avantage Data System software (Thermo Scientific, China). The final fitting results of the O 1s spectra for the unaged sample are presented in Fig. 6(b) as an example. A satisfying consistency is reached between the measured data and the fitted results. O 1s(I) and O 1s(II) are reported to be associated with oxygen adsorption and oxygen lattice, respectively [37–39]. Therefore, they are described as O$_{adsorption}$ and O$_{lattice}$, respectively, in the following part for simplicity.

Figures 7(a)–7(c) show the normalized depth profiles of the amount of O$_{adsorption}$ and O$_{lattice}$ at the GB of unaged sample, the sample recovered after aged in air, and the sample recovered after aged in nitrogen. For the unaged sample, there is a clear accumulation of O$_{adsorption}$ at the GB, which gradually decreases as the O$_{lattice}$ becomes dominant due to etching into the grain [2].

Similar results are also observed in the sample recovered after aged in air, which implies that the amount of O$_{adsorption}$ at the GB could stay steady during aging in air. The almost unchanged GB oxygen distribution is in consistent with their totally recovered electrical properties, supporting the existence of stable interface states in stable samples [25,26]. The nitrogen atmosphere, however, could facilitate the consumption of O$_{adsorption}$. The sample recovered after aged in nitrogen has significantly consumed O$_{adsorption}$ at the GB, which shows a completely different variation trend from the former two cases, as shown in Fig. 7(c). The recovery at the aging temperature could barely help the sample regain the consumed O$_{adsorption}$.

The consumption of O$_{adsorption}$ leads to severe electrical degradation by resulting in deterioration in interface states and deformation in DSB. It could be schematically illustrated by the diagram (Fig. 7(d)). The oxygen-deficient atmosphere makes the negatively charged O$_{adsorption}$, which might have two charged states (O$'_{adsorption}$ and O$''_{adsorption}$), could easily combine with positively charge mobile ions, e.g., Zn$_i^{\cdot}$ and Zn$_i^{\cdot\cdot}$, thus forming ZnO lattices at the GB. The neutralization
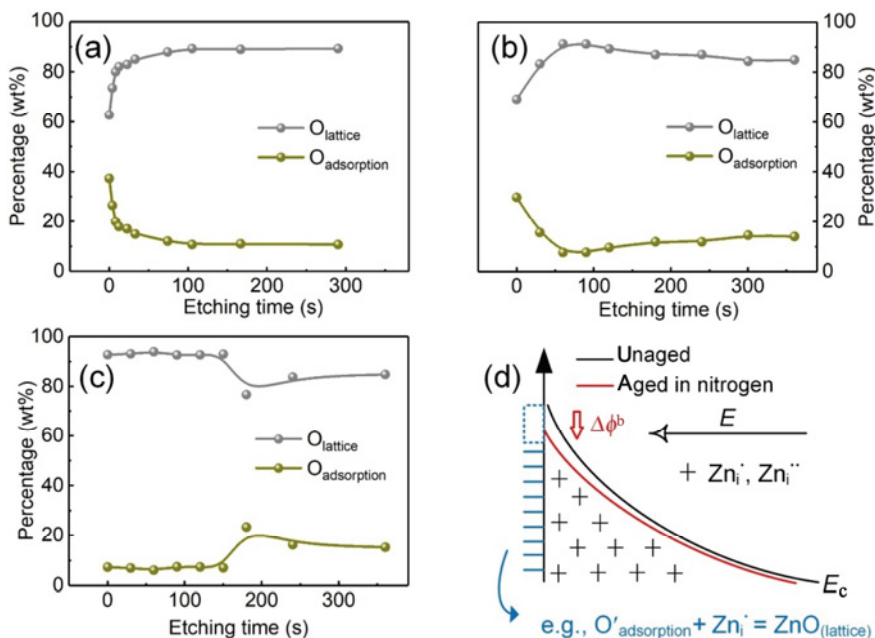
Fig. 7 Dependence of normalized weight percentages of GB $O_{adsorption}$ and $O_{lattice}$ on etching time: (a) unaged, (b) recovered after aged in air, and (c) recovered after aged in nitrogen. (d) Transition from $O_{adsorption}$ to $O_{lattice}$ due to aging in nitrogen. Note: E_c is the energy at the conduction band, and $\Delta\phi_b$ is the variation of barrier height.

subsequently contributes to the decrease in the N_i, leading to the lowered ϕ_b of the DSB [2]. Overall, the long-term stability of stable ZnO varistor ceramics undoubtedly depends on their steady amount of $O_{adsorption}$ at the GB.

3.3 Distribution of interface states $N_i(E)$

The above results suggest that the consumption of $O_{adsorption}$ could lead to a detrimental degradation of stable ZnO varistor ceramics by reducing the N_i. However, the interpretation is still at the level of a qualitative description of N_i. Therefore, we attempt to gain a thorough understanding by characterizing the dynamics of the $N_i(E)$. Many techniques have been proposed to investigate the interface states of ZnO varistor ceramics, such as deep level transient spectroscopy (DLTS) [40], dielectric spectroscopy [11], capacitance–voltage technique [41], and the deconvolution method based on nonlinear J–E characteristics [42]. In this study, the J–E deconvolution method combined with the capacitance–voltage technique was used to obtain the $N_i(E)$. It should be noted that this method assumes uniformly distributed depletion layers. Therefore, only unaged and sufficiently recovered samples are used for further analysis.

For the capacitance–voltage measurement, when a DC voltage is applied on the sample, the GB capacitance

per unit area C decreases with an increase in the voltage drop on the GB U_{gb} [43–45].

$$\left(\frac{1}{C} - \frac{1}{2C_0}\right)^2 = \frac{2}{q\varepsilon_0\varepsilon_r N_d}(\phi_b + U_{gb}) \tag{2}$$

with

$$\frac{1}{C_0} = 2\left(\frac{2\phi_b}{q\varepsilon_0\varepsilon_r N_d}\right)^{1/2} \tag{3}$$

where C_0 is the zero-biased C, ε_0 is the vacuum permittivity, ε_r is the relative permittivity of ZnO, and N_d is the donor density. C was measured at 10^4 Hz to eliminate the DC conduction. U_{gb} is obtained by using $U_{gb} = U/U_{1mA}U_{b\_ZnO}$, where U_{b_ZnO} (= 3.2 V) is generally acknowledged as the breakdown voltage of a single DSB [2,46].

Dependencies of C on U_{gb} for unaged and recovered samples are shown in Fig. 8, where $(C^{-1} - 0.5\,C_0^{-1})^2$ and U_{gb} are linearly fitted. As presented in Fig. 8(a), complete recovery is observed in the capacitance–voltage characteristics of the sample aged in air. The donor densities of the unaged sample and the sample recovered after aged in air are both calculated as 4.43×10^{23} m^{-3} according to Eq. (2). On the other hand, for the sample recovered after aged in nitrogen, noticeable reduction in their N_d is observed in Fig. 8(b), which drops from 4.43×10^{23} to 4.24×10^{23} m^{-3} even
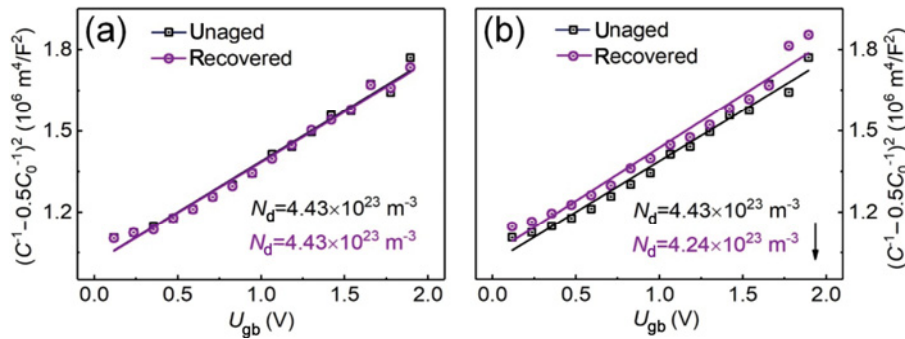
Fig. 8 $(C^{-1} - 0.5 C_0^{-1})^2$ vs. U_{gb} characteristics: (a) unaged and recovered for 509 h after aged in air and (b) unaged and recovered for 540 h after aged in nitrogen.

after 540 h of recovery. The unchanged N_d could also be supported by their totally recovered nonlinear *J–E* characteristics, the dielectric spectroscopy results, and the simulation results [25]. It essentially originates from the stable interface states, which do not combine with mobile donor ions during aging in air [25,26]. According to Fig. 8(b), the stable interface states correlate with the unchanged GB $O_{adsorption}$, which, however, would combine with positive mobile ions like $Zn_i^·$ during being aged in nitrogen. Unfortunately, the reason why the GB $O_{adsorption}$ and the related interface states could remain stable is still unclear, which needs more work in the future.

The electron filling of $N_i(E)$ determines the interfacial charge Q_i. As a result, $N_i(E)$ could be deconvoluted by the deviation of Q_i [42,47].

$$N_i(E) = \frac{dQ_i(E)}{dE} \qquad (4)$$

where E is fixed with respect to the valence band. The band gap E_g of the DSB is given as 3.16 eV. The negatively charged Q_i is balanced by the positively charged depletion charges according to the charge conservation law.

$$Q_i = x_F N_d + x_R N_d \qquad (5)$$

where x_F and x_R are the widths of the forward and reverse depletion layers, respectively. They represent the compression and expansion of the DSB by the biased DC voltage, respectively. x_F and x_R can be solved by the DSB model proposed by Blatter and Greuter [12]. The band diagram of a DSB is shown in Fig. 9. For the sake of simplicity, only shallow bulk traps are included. The excellent nonlinear *J–E* characteristics of ZnO varistor ceramics are contributed by those unoccupied empty interface states, which are important for the pinning of the potential barrier
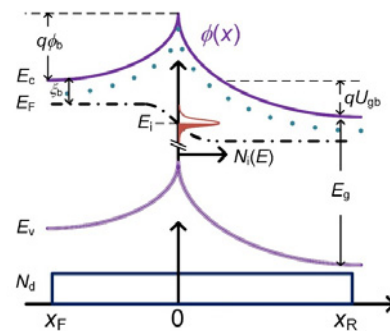
Fig. 9 Band diagram of DSB. Note: E_i is the quasi-Fermi level, E_F and E_v are the energy at the Fermi level and valence band, respectively, and $\phi(x)$ is the potential distribution.

against the U [2].

On the assumption of uniformly distributed depletion layers, the $\phi(x)$ of the DSB can be calculated by Eq. (6) [12]:

$$\phi(x) = \begin{cases} \dfrac{qN_d}{2\varepsilon_0\varepsilon_r}(x + x_F)^2, & -x_F \leqslant x \leqslant 0 \\[2mm] \dfrac{qN_d}{2\varepsilon_0\varepsilon_r}(x - x_R)^2 - U_{gb}, & 0 \leqslant x \leqslant x_R \end{cases} \qquad (6)$$

The GB potential $\phi(0)$ is equal to ϕ_b, which can be derived by Eq. (7) according to Eq. (1) [12]:

$$\phi_b(U_{gb}) = \frac{kT}{q} \ln\left(\frac{A^* T^2}{J}\right)\left(1 - e^{-\frac{qU_{gb}}{kT}}\right) - \frac{\xi_b}{q} \qquad (7)$$

The solutions of x_F and x_R, subject to Eqs. (6) and (7), are given by Eq. (8):

$$x_F = \left(\frac{2\varepsilon_0\varepsilon_r}{qN_d}\phi_b\right)^{1/2}, \quad x_R = \left[\frac{2\varepsilon_0\varepsilon_r}{qN_d}(\phi_b + U_{gb})\right]^{1/2} \qquad (8)$$

Therefore, $N_i(E)$ could be deconvoluted by solving Eqs. (4), (5), and (8).

The deconvolution results are demonstrated in Fig. 10.

The sample recovered after aged in air exhibits similar results to the unaged one, supporting its total recovery as well. As for the sample aged in nitrogen, irreversibility is observed. As shown in Fig. 10(b1), the ϕ_b in the low-voltage region is reduced, which corresponds to the increase in J_L, as shown in Fig. 4(c1) according to Eq. (1). Figure 10(b2) shows the decreased Q_i at the same energy level. In particular, the saturated Q_i at E_i = 2.4 eV drops, suggesting the decrease in the N_i (= Q_{imax}/q, where Q_{imax} is the maximum interfacial charge). It also agrees with the decrease in N_d. In addition, the distributions of interface states (Fig. 10(b3)) are significantly distorted, which represents the consumption of interface states at different energy levels.

Since interface states are composed of different energy levels, the results in Figs. 10(a3) and 10(b3) are further decomposed in Figs. 11(a) and 11(b),

respectively. The unoccupied parts, i.e., $N_{i2}(E)$ and $N_{i3}(E)$, which have already been presented by the J–E deconvolution method, are fitted by assuming the Gaussian distribution of interface states. The fully occupied part, which does not respond to the U_{gb}, is fitted by their $\phi_b(U_{gb})$ curves. The sum of the densities of these three states is calculated to meet their saturated Q_i, i.e., $Q_{imax}/q = N_i = \sum N_{i(n)}$. Finally, three distributions of interface states, $N_{i1}(E)$, $N_{i2}(E)$, and $N_{i3}(E)$, are decomposed, which are centered at 1.91, 2.13, and 2.20 eV, respectively. Among them, $N_{i3}(E)$ has been reported in Ref. [2]. The detailed fitting results are presented in Table 1. The recovered sample previously aged in air shows nearly identical interface states with the unaged sample. On the other hand, the total interface density of the sample recovered after aged in nitrogen drops from 5.73×10^{16} to 5.52×10^{16} e/(eV·m²). Particularly, the reduction almost comes
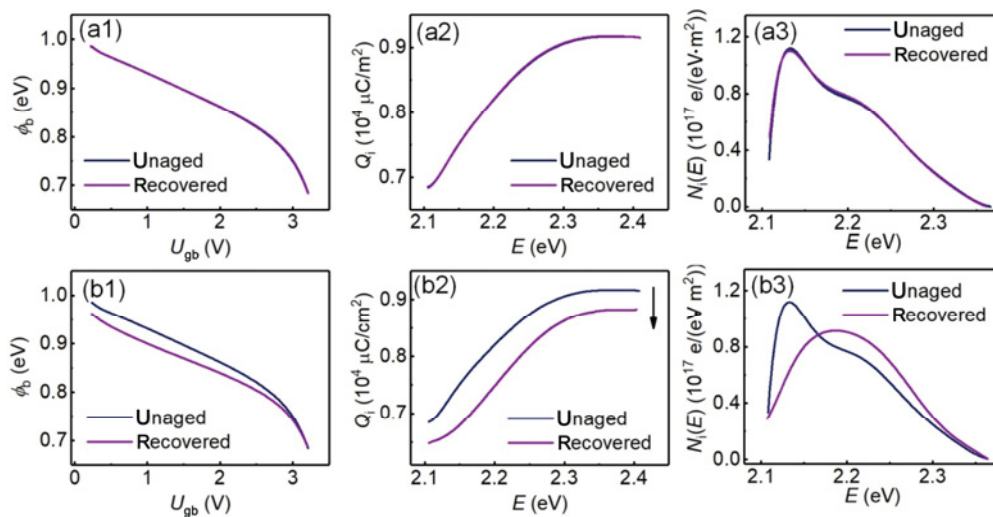
Fig. 10 ϕ_b vs. U_{gb}: (a1) unaged and recovered for 509 h after aged in air and (b1) unaged and recovered for 540 h after aged in nitrogen. Q_i vs. E_i: (a2) unaged and recovered for 509 h after aged in air and (b2) unaged and recovered for 540 h after aged in nitrogen. N_i vs. E_i: (a3) unaged and recovered for 509 h after aged in air and (b3) unaged and recovered for 540 h after aged in nitrogen.
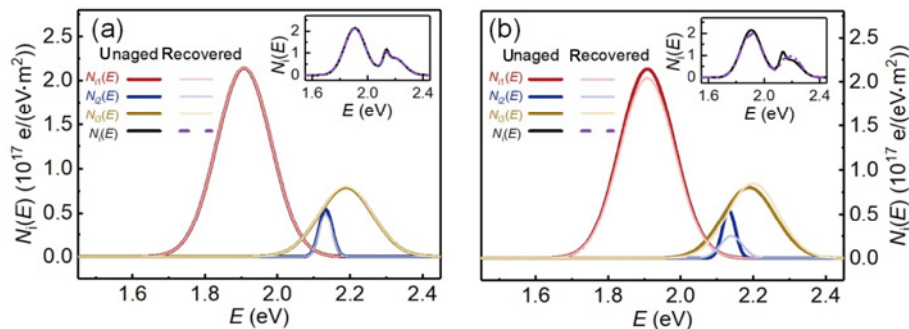
Fig. 11 Decomposed distributions of $N_i(E)$: (a) unaged and recovered for 509 h after aged in air and (b) unaged and recovered for 540 h after aged in nitrogen. The insets are the comparison of the unaged and recovered $N_i(E)$, where the black lines and the purple lines represent the unaged $N_i(E)$ and the recovered $N_i(E)$, respectively.

Table 1 Decomposed densities of interface states

Sample	DOS (10^{16} e/(eV·m^2))			
	N_{i1}	N_{i2}	N_{i3}	N_i
Unaged	4.02	0.25	1.46	5.73
Recovered after aged in air	3.92	0.22	1.48	5.73
Recovered after aged in nitrogen	3.84	0.19	1.49	5.52

from N_{i1} and N_{i2}, which decrease from 4.02×10^{16} to 3.84×10^{16} e/(eV·m^2) and from 0.25×10^{16} to 0.19×10^{16} e/(eV·m^2), respectively. The decreases in the densities of the two lower-lying states, N_{i1} and N_{i2}, are also in accordance with the irreversible degradation of the low-voltage region, as shown in Figs. 4(c) and 10(b). Moreover, their decrements are believed to be closely related to the consumption of O$_{adsorption}$ at GBs, which directly leads to the degradation of the DSB.

4 Conclusions

In conclusion, atmospheric DC aging in air and nitrogen is used to investigate the aging nature of modern stable ZnO varistor ceramics. In comparison to decreasing the power loss in air, aging in nitrogen would result in a continuous increase in power loss and severe electrical degradation in about 50 h, i.e., α dropping from 23.0 to 6.7 and J_L rising from 22.5 to 118.5 mA/cm^2. The long-term stability is destructed in nitrogen, as their electrical properties could not be recovered even after 540 h. The transition of power loss is unveiled by their GB depth profiles, as oxygen adsorption at the GB would convert to oxygen lattice in nitrogen but keep stable in air. Moreover, the N_i, which contributes to the pinning of ϕ_b during aging, decreases in nitrogen. The N_i drops from 5.73×10^{16} e/(eV·m^2) for the unaged sample to 5.52×10^{16} e/(eV·m^2) for the sample recovered after aged in nitrogen. However, the sample aged in air shows a steady amount of oxygen adsorption at the GB and stable interface states, which might account for their excellent long-term stability and reversible electrical properties. Reasonably, the stable existence of oxygen adsorption at the GB could be the key to creating stable interface states, thereby contributing to the excellent long-term stability of stable samples. Therefore, revising the stability of oxygen adsorption is suggested as a possible avenue for improving the aging performance of ZnO varistor ceramics.

Declaration of competing interest

The authors have no competing interests to declare that are relevant to the content of this article.

References

[1] Gupta TK. Application of zinc oxide varistors. *J Am Ceram Soc* 1990, **73**: 1817–1840.

[2] Greuter F. ZnO varistors: From grain boundaries to power applications. In: *Oxide Electronics*. Ray A, Ed. Chichester, UK: John Wiley & Sons, Ltd., 2021: 157–234.

[3] Tian T, Zheng LY, Podlogar M, *et al*. Novel ultrahigh-performance ZnO-based varistor ceramics. *ACS Appl Mater Interfaces* 2021, **13**: 35924–35929.

[4] Ramírez MA, Simões AZ, Bueno PR, *et al*. Importance of oxygen atmosphere to recover the ZnO-based varistors properties. *J Mater Sci* 2006, **41**: 6221–6227.

[5] He JL, Cheng CL, Hu J. Electrical degradation of double-Schottky barrier in ZnO varistors. *AIP Adv* 2016, **6**: 030701.

[6] Gupta TK, Carlson WG. A grain-boundary defect model for instability/stability of a ZnO varistor. *J Mater Sci* 1985, **20**: 3487–3500.

[7] CIGRE Working Group A3.17. Metal oxide (MO) surge arresters-Stresses and test procedures. Reference: 544, 2013.

[8] CIGRE Working Group A3.25. MO surge arresters: Metal oxide resistors and surge arresters for emerging system conditions. Reference: 696, 2017.

[9] Long YW, Gao J, Cheng ZL, *et al*. Skin–core structure of thermally aged epoxy resin: Roles of oxidation and re-crosslinking. *Polym Degrad Stabil* 2021, **193**: 109743.

[10] International Electrotechnical Commission. IEC 60099-4 Surge arresters—Part 4: Metal-oxide surge arresters without gaps for a.c. systems. IEC, 2014.

[11] Greuter F, Blatter G. Electrical properties of grain boundaries in polycrystalline compound semiconductors. *Semicond Sci Tech* 1990, **5**: 111–137.

[12] Blatter G, Greuter F. Carrier transport through grain boundaries in semiconductors. *Phys Rev B* 1986, **33**: 3952–3966.

[13] Wang C, Zhao XT, Ren LL, *et al*. Enhanced dielectric and

energy storage properties of P(VDF–HFP) through elevating β-phase formation under unipolar nanosecond electric pulses. *Appl Phys Lett* 2023, **122**: 023903.

[14] Gao J, Wu KN, Li JY, *et al*. All-organic lead-free thermochromic and dielectric switchable epoxy microcomposites from singly incorporating leuco dye microcapsules for advanced encryption. *Smart Mater Struct* 2023, **32**: 015019.

[15] Clarke DR. Varistor ceramics. *J Am Ceram Soc* 1999, **82**: 485–502.

[16] Boonlakhorn J, Chanlek N, Manyam J, *et al*. Enhanced giant dielectric properties and improved nonlinear electrical response in acceptor-donor (Al^{3+}, Ta^{5+})-substituted $CaCu_3Ti_4O_{12}$ ceramics. *J Adv Ceram* 2021, **10**: 1243–1255.

[17] Lee J, Choi Y, Park BJ, *et al*. Precise control of surface oxygen vacancies in ZnO nanoparticles for extremely high acetone sensing response. *J Adv Ceram* 2022, **11**: 769–783.

[18] Wu KN, Li R, Jia R, *et al*. Transition of the colossal permittivity related dielectric relaxation in V-doped $CaCu_3Ti_4O_{12}$ ceramics. *J Appl Phys* 2022, **132**: 164103.

[19] Wu KN, Huang YW, Li JY, *et al*. Space charge polarization modulated instability of low frequency permittivity in $CaCu_3Ti_4O_{12}$ ceramics. *Appl Phys Lett* 2017, **111**: 042902.

[20] Chen X, Li GR, Tian T, *et al*. Microstructural and electrical features of highly conducting indium co-doped ZnO-based ceramics. *J Am Ceram Soc* 2022, **105**: 6680–6692.

[21] Yang X, Hu J, Wang SJ, *et al*. A dielectric polymer/metal oxide nanowire composite for self-adaptive charge release. *Nano Lett* 2022, **22**: 5167–5174.

[22] Liu RZ, Chen ZW, Lu ZY, *et al*. Effects of sintering temperature and Bi_2O_3, Y_2O_3 and MgO co-doping on the dielectric properties of X8R $BaTiO_3$-based ceramics. *Ceram Int* 2022, **48**: 2377–2384.

[23] Guo M, Zhao X, Shi WD, *et al*. Simultaneously improving the electrical properties and long-term stability of ZnO varistor ceramics by reversely manipulating intrinsic point defects. *J Eur Ceram Soc* 2022, **42**: 162–168.

[24] Huang YW, Wu KN, Xing ZL, *et al*. Understanding the validity of impedance and modulus spectroscopy on exploring electrical heterogeneity in dielectric ceramics. *J Appl Phys* 2019, **125**: 084103.

[25] Cheng ZL, Hou ZK, Wang Y, *et al*. Steadily decreasing power loss of a double Schottky barrier originating from the dynamics of mobile ions with stable interface states. *Phys Rev Applied* 2022, **17**: 034042.

[26] Wu KN, Hou ZK, Cheng ZL, *et al*. Revisiting the feasibility of distinguishing the long-term stability of MOVs by power loss. *IEEE T Dielect El In* 2022, **29**: 1983–1990.

[27] Peng P, Deng YJ, Niu JP, *et al*. Fabrication and electrical characteristics of flash-sintered SiO_2-doped ZnO–Bi_2O_3–MnO_2 varistors. *J Adv Ceram* 2020, **9**: 683–692.

[28] Bueno PR, Leite ER, Oliveira MM, *et al*. Role of oxygen at the grain boundary of metal oxide varistors: A potential barrier formation mechanism. *Appl Phys Lett* 2001, **79**: 48–50.

[29] Stucki F, Greuter F. Key role of oxygen at zinc oxide varistor grain boundaries. *Appl Phys Lett* 1990, **57**: 446–448.

[30] Wu KN, Wang Y, Hou ZK, *et al*. Colossal permittivity due to electron trapping behaviors at the edge of double Schottky barrier. *J Phys D Appl Phys* 2021, **54**: 045301.

[31] Meng PF, Yang X, Wu JB, *et al*. Stable electrical properties of ZnO varistor ceramics with multiple additives against the AC accelerated aging process. *Ceram Int* 2019, **45**: 11105–11108.

[32] Wang X, Ren X, Li ZY, *et al*. A unique tuning effect of Mg on grain boundaries and grains of ZnO varistor ceramics. *J Eur Ceram Soc* 2021, **41**: 2633–2640.

[33] Cao WB, Xie X, Wang YQ, *et al*. Effect of Pr_6O_{11} doping on the microstructure and electrical properties of ZnO varistors. *Ceram Int* 2019, **45**: 24777–24783.

[34] Guo M, Wang Y, Wu KN, *et al*. Revisiting the effects of Co_2O_3 on multiscale defect structures and relevant electrical properties in ZnO varistors. *High Volt* 2020, **5**: 241–248.

[35] Caglar Y, Caglar M, Ilican S. XRD, SEM, XPS studies of Sb doped ZnO films and electrical properties of its based Schottky diodes. *Optik* 2018, **164**: 424–432.

[36] Honma T, Sato R, Benino Y, *et al*. Electronic polarizability, optical basicity and XPS spectra of Sb_2O_3–B_2O_3 glasses. *J Non-Cryst Solids* 2000, **272**: 1–13.

[37] Ma Q, Ogino A, Matsuda T, *et al*. Cathodoluminescence property of ZnO nano-phosphors fabricated by pulsed Nd:YAG laser ablation in plasma circumstance. *Thin Solid Films* 2010, **518**: 3517–3521.

[38] Lv W, Wei B, Xu LL, *et al*. Photocatalytic properties of hierarchical ZnO flowers synthesized by a sucrose-assisted hydrothermal method. *Appl Surf Sci* 2012, **259**: 557–561.

[39] Islam MN, Ghosh TB, Chopra KL, *et al*. XPS and X-ray diffraction studies of aluminum-doped zinc oxide transparent conducting films. *Thin Solid Films* 1996, **280**: 20–25.

[40] Tsuda K, Mukae K. Characterization of the interface states in ZnO varistors by DLTS method. *J Ceram Soc Jpn* 1989, **97**: 1211–1218.

[41] Ohbuchi Y, Kawahara T, Okamoto Y, *et al*. Characterization of interface states in degraded ZnO varistors. *Jpn J Appl Phys* 2002, **41**: 190–196.

[42] Greuter F, Blatter G, Rossinelli M, *et al*. Bulk and grain boundary defects in polycrystalline ZnO. *Mater Sci Forum* 1986, **10–12**: 235–240.

[43] Mukae K, Tsuda K, Nagasawa I. Capacitance-vs-voltage characteristics of ZnO varistors. *J Appl Phys* 1979, **50**: 4475–4476.

[44] Jiang HB, Ren X, Lao XB, *et al*. Effect of NiO doping on grain growth and electrical properties of ZnO-based varistors. *J Eur Ceram Soc* 2022, **42**: 3898–3904.

[45] Cheng XZ, Lu ZY, Liu XY, *et al*. Improvement of surge current performances of ZnO varistor ceramics via C_3N_4-doping. *J Eur Ceram Soc* 2020, **40**: 2390–2395.

[46] Cheng ZL, Hou ZK, Wu T, *et al*. Transient conduction of ZnO varistors under moderate time-varying voltages:

   Dynamics of interfacial charges of the double Schottky barrier. *J Appl Phys* 2023, **133**: 054101.

[47] Tang Z, Ning K, Fu ZY, *et al*. Significantly enhanced varistor properties of CaCu$_3$Ti$_4$O$_{12}$ based ceramics by designing superior grain boundary: Deepening and broadening interface states. *J Mater Sci Technol* 2022, **108**: 82–89.